

# SCIENTIFIC REPORTS

OPEN

## Fabrication of Wide-Range-Visible Photocatalyst $\text{Bi}_2\text{WO}_{6-x}$ nanoplates via Surface Oxygen Vacancies

Yanhui Lv<sup>1,2</sup>, Wenqing Yao<sup>1</sup>, Ruilong Zong<sup>1</sup> & Yongfa Zhu<sup>1</sup>

Received: 06 July 2015

Accepted: 07 December 2015

Published: 18 January 2016

$\text{Bi}_2\text{WO}_6$  as a high visible-light-driven catalyst has been aroused broad interest. However, it can only be excited by the light with  $\lambda < 450 \text{ nm}$  and the solar energy utilization need to be improved. Here, the wide-range-visible photoresponse  $\text{Bi}_2\text{WO}_{6-x}$  nanoplates were fabricated by introducing surface oxygen vacancies through the controllable hydrogen reduction method. The visible photoresponse wavelength range is extended from 450 nm to more than 600 nm. In addition, the photocatalytic activity of  $\text{Bi}_2\text{WO}_{6-x}$  is also increased and is 2.1 times as high as that of pristine  $\text{Bi}_2\text{WO}_6$ . The extending of the photoresponse range and the enhancement of the photoactivity both can be attributed to the surface-oxygen-vacancy states. This is because surface-oxygen-vacancy states generated above and partly overlapping of with the valence band (VB) will result in the rising of valence band maximum (VBM), thus broadening the VB width. This approach is proposed to develop many types of wide-range-visible optical materials and to be applicable to many narrow and wide bandgap materials.

For decades, photocatalysis as a green chemistry technology using sunlight has been attracting tremendous attention. Photocatalysis can completely decompose organic pollutants even at low levels in an ambient environment.  $\text{Bi}_2\text{WO}_6$  has attracted considerable attention for its physical and chemical properties, such as pyroelectricity, ferroelectricity, piezoelectricity and non-linear dielectric susceptibility<sup>1–7</sup>. Besides,  $\text{Bi}_2\text{WO}_6$  is also a kind of excellent visible-light-driven photocatalysts on the degradation of organic pollutants and water splitting ( $\text{O}_2$  evolution)<sup>8–14</sup>. The high photoactivity of  $\text{Bi}_2\text{WO}_6$  could be attributed to the corner-sharing structure of  $\text{WO}_6$  octahedron sandwiched between  $(\text{Bi}_2\text{O}_2)^{2+}$  layers, which is conducive to the transfer of electrons to the surface of the photocatalyst along the layered network because the recombination of photogenerated electron and hole pairs can be suppressed by the electron transferring to a layered host<sup>11,12,15</sup>. Kudo and Hiji first reported the photocatalytic  $\text{O}_2$  evolution by  $\text{Bi}_2\text{WO}_6$  from  $\text{AgNO}_3$  solution<sup>11</sup>. Zou and Ye *et al.* demonstrated that  $\text{Bi}_2\text{WO}_6$  possessed the photocatalytic activity for  $\text{O}_2$  evolution, as well as the activity of mineralizing both  $\text{CHCl}_3$  and  $\text{CH}_3\text{CHO}$  to  $\text{CO}_2$  under visible-light irradiation<sup>12</sup>. Furthermore, in order to increase the utilization efficiency of sunlight, many works have been researched on the enhanced of photoactivity, such as  $\text{F-Bi}_2\text{WO}_6$ <sup>10</sup>,  $\text{Co}_3\text{O}_4\text{-Bi}_2\text{WO}_6$ <sup>16</sup>,  $\text{AgBr-Ag-Bi}_2\text{WO}_6$ <sup>17</sup>,  $\text{Er}^{3+}\text{-Bi}_2\text{WO}_6$ <sup>18</sup>,  $\text{Gd-Bi}_2\text{WO}_6$ <sup>19</sup>,  $\text{C}_{60}\text{-Bi}_2\text{WO}_6$ <sup>20</sup>,  $\text{C-Bi}_2\text{WO}_6$ <sup>21</sup>,  $\text{Ag-Bi}_2\text{WO}_6$ <sup>22</sup>, Ce and F codoped  $\text{Bi}_2\text{WO}_6$ <sup>23</sup> etc. However, these composite photocatalysts either contain toxic ions ( $\text{Co}^{3+}$ ) or are expensive ( $\text{Er}^{3+}$ ,  $\text{C}_{60}$ , Ag) or possess complex synthetic process. Therefore, it is still a great challenge to find a facile, economical, environmentally benign method to fabricate high-efficient  $\text{Bi}_2\text{WO}_6$ -based photocatalysts. It is well known that the defect structure is one of the important factors on the photocatalytic performance. Recently, some works have been founded that the amazing generation of the visible photoactivity for the UV lighted photocatalyst (mainly  $\text{TiO}_2$  and  $\text{ZnO}$ ) by introducing oxygen vacancies<sup>24–27</sup>. In our previous work, simple semiconductor  $\text{ZnO}$  and high UV photoactivity  $\text{BiPO}_4$  photocatalysts with surface oxygen vacancies were successfully fabricated via two facile, economical and highly efficient methods, vacuum deoxidation and controllable hydrogen reduction<sup>28–30</sup>. After surface oxygen vacancies were introduced in the photocatalyst, the photoresponse wavelength range is extended as well as the UV photoactivity is greatly improved.

In this work,  $\text{Bi}_2\text{WO}_{6-x}$  photocatalyst with wide-range-visible response and high-visible activity was fabricated by introducing surface oxygen vacancies. The formation process of oxygen vacancies has been discussed in detail, and the influences of the oxygen vacancy extent on the photoabsorption properties, electric potential

<sup>1</sup>Department of Chemistry, Beijing Key Laboratory for Analytical Methods and Instrumentation, Tsinghua University, Beijing, 100084, People's Republic of China. <sup>2</sup>Key Laboratory of Photochemistry Beijing National Laboratory for Molecular Sciences Institute of Chemistry, Chinese Academy of Sciences, Beijing 100190, People's Republic of China. Correspondence and requests for materials should be addressed to Y.Z. (email: zhuyf@tsinghua.edu.cn)

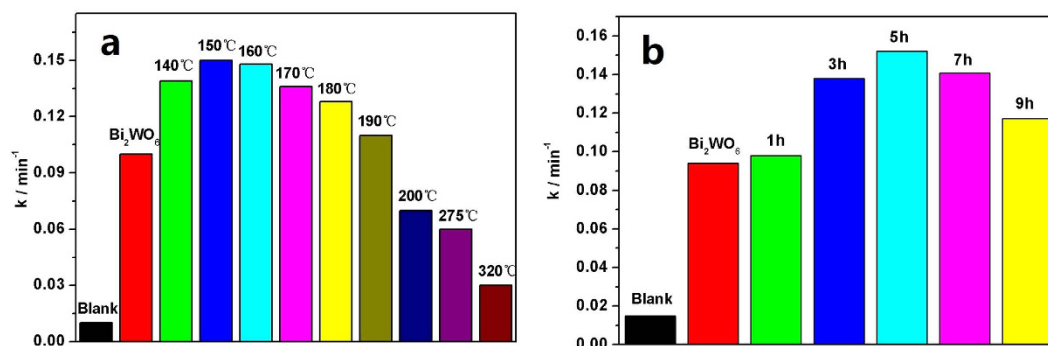


**Figure 1.** Visible Photocatalytic activity of pristine  $\text{Bi}_2\text{WO}_6$  and  $\text{Bi}_2\text{WO}_{6-x}$  after hydrogen reduction (a) at various temperature for 5 h; (b) at 150 °C for various time on the degradation of 2, 4-DCP,  $\lambda > 420 \text{ nm}$ .

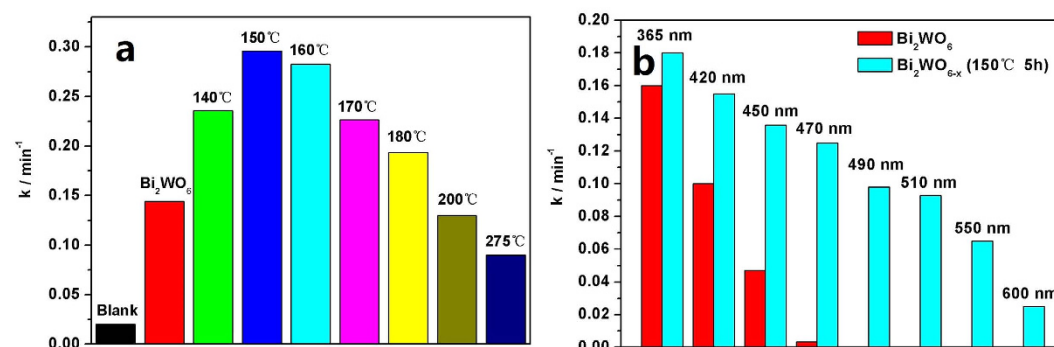


**Figure 2.** (a) The simulated solar photocatalytic activities of  $\text{Bi}_2\text{WO}_6$  and  $\text{Bi}_2\text{WO}_{6-x}$  samples after hydrogen reduction at various temperatures for 5 h on the degradation of 2, 4-DCP, under 500 W Xe lamp with an AM1.5 filter; (b) The photoactivities of  $\text{Bi}_2\text{WO}_6$  and  $\text{Bi}_2\text{WO}_{6-x}$  samples on the degradation of 2, 4-DCP, under different wavelength irradiation.

and electronic structure also have been investigated. The roundly mechanism of the increased photocatalytic efficiency and activity has been provided. Furthermore, this work is a supplement for illustrating that it is a universal way that can extend the photoresponse range as well as enhance photoactivity by introducing surface oxygen vacancies.

## Results and Discussions

**Enhancement of Photocatalytic Activity.** Visible photocatalytic activities of  $\text{Bi}_2\text{WO}_6$  and  $\text{Bi}_2\text{WO}_{6-x}$  samples after hydrogen treated with various temperature for 5 h and various time at 150 °C on the degradation of 2, 4-dichlorophenol (2, 4-DCP), under  $\lambda > 420 \text{ nm}$  light, are shown in Fig. 1a,b. The degradation process is fitted to pseudo-first-order kinetics, and the value of the rate constant  $k$  is equal to the corresponding slope of the fitting line. The visible photocatalytic activities of  $\text{Bi}_2\text{WO}_{6-x}$  samples gradually enhanced with the increase of hydrogen reduction temperature and time; when the temperature reaches 150 °C, time is for 5 h,  $\text{Bi}_2\text{WO}_{6-x}$  displays the highest photodegradation activity. The apparent rate constant  $k$  is  $0.152 \text{ min}^{-1}$  and it is about 1.6 times as high as that of pristine  $\text{Bi}_2\text{WO}_6$  ( $k = 0.093 \text{ min}^{-1}$ ). However, further increasing the temperature or prolonging the time, the degradation rate begins to decrease. Even when the temperature is higher than 200 °C (such as at 275, 320 °C), the photoactivity of  $\text{Bi}_2\text{WO}_{6-x}$  is lower than that of pristine  $\text{Bi}_2\text{WO}_6$ . The photocatalytic performance of  $\text{Bi}_2\text{WO}_{6-x}$  photocatalysts are greatly influenced by the number and kind of oxygen vacancies and the reduction degree of  $\text{Bi}_2\text{WO}_6$  (for example after 320 °C, 5 h hydrogen reduction, metal Bi is generated), which are controlled by tuning the temperature and time in the process of hydrogen reduction. As is well known, high concentration of surface oxygen vacancies contribute to the separation efficiency of photogenerated electron-hole pairs, improving the photocatalytic activity; while bulk oxygen vacancies as charge capture center will inhibit the photoactivity<sup>31</sup>. In addition, metal Bi has no photocatalytic activity, and its existence is infaust for the photocatalytic performance of  $\text{Bi}_2\text{WO}_6$ <sup>32</sup>.

Fig. 2a shows the simulated sunlight photocatalytic performance of  $\text{Bi}_2\text{WO}_6$  and  $\text{Bi}_2\text{WO}_{6-x}$  samples on the degradation of 2, 4-DCP, utilizing 500 W Xe lamp an AM1.5 filter. It can be seen that the influence law of the temperature on the photocatalytic activity is the same as that under visible light. The photoactivities of  $\text{Bi}_2\text{WO}_{6-x}$  samples firstly increase and then begin to decline with the increased of the hydrogen reduction temperature. However, the difference here is the apparent rate constant  $k$  of  $\text{Bi}_2\text{WO}_{6-x}$  reduction at 150 °C is to  $0.30 \text{ min}^{-1}$  and

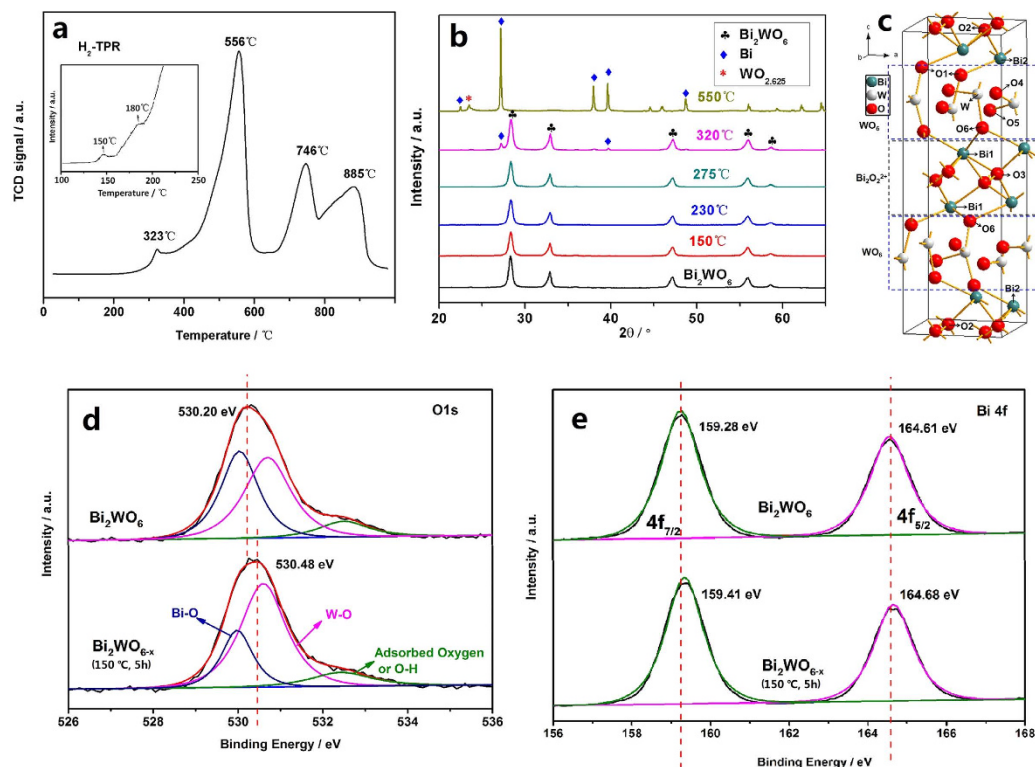


**Figure 3.** (a)  $H_2$ -TPR profile of  $Bi_2WO_6$  sample, the inset shows an enlarged TCD signal; (b) The XRD spectra of  $Bi_2WO_6$  and  $Bi_2WO_{6-x}$  samples; (c) The unit cell of  $Bi_2WO_6$ . Blue, white and red spheres represent Bi, W and O atoms; (d) O 1s XPS spectra of  $Bi_2WO_6$  and  $Bi_2WO_{6-x}$  (150 °C, 5 h) samples. The red curve is the fitting of experimental data for samples, which is decomposed into a superposition of three peaks shown as blue, pink and green curves; (e) Bi 4f XPS spectra of  $Bi_2WO_6$  and  $Bi_2WO_{6-x}$  (150 °C, 5 h) samples.

Sample	Bi4f	W4f	O1s	Bi4f:W4f:O1s
$Bi_2WO_6$	16.53	6.35	50.87	1:0.384:3.07
$Bi_2WO_{6-x}$ (150 °C, 5 h)	16.65	6.42	48.29	1:0.385:2.90

**Table 1.** Surface atomic concentration of  $Bi_2WO_6$  and  $Bi_2WO_{6-x}$  (150 °C, 5 h) come from XPS.

it is about 2.1 times as high as that of pristine  $Bi_2WO_6$ , which is higher than that under visible light (1.6 times). This indicates that the UV photoactivity of  $Bi_2WO_{6-x}$  is improved, which can also be testified via the increased UV photoactivity of  $Bi_2WO_{6-x}$  on the degradation of 2, 4-DCP under  $\lambda = 365$  nm light, as shown in Fig. 2b.

To further investigate the extending of visible photoresponse range of  $Bi_2WO_{6-x}$  (150 °C, 5 h), the photocatalytic performances on the degradation of 2, 4-DCP of it and pristine  $Bi_2WO_6$  were investigated, under 500 W Xe lamp with different wavelength filter (Fig. 2b). It can be found that the photoactivity of  $Bi_2WO_{6-x}$  shows visibly higher than that of pristine  $Bi_2WO_6$  under  $\lambda < 450$  nm. And the longer of the incident light wavelength, the higher of the enhanced photoactivity of  $Bi_2WO_{6-x}$  (150 °C, 5 h). Since the energy band gap of pristine  $Bi_2WO_6$  is about 2.8 eV, it cannot be excited by the light with  $\lambda > 470$  nm, thus it has hardly photocatalytic activity under 470 nm light irradiation. However,  $Bi_2WO_{6-x}$  (150 °C, 5 h) photocatalyst shows distinctly photocatalytic activity ( $\lambda > 470$  nm). Even under  $\lambda > 600$  nm irradiation, it still exhibits observable photoactivity. In sum, the visible photoresponse range is extended from 450 nm for pristine  $Bi_2WO_6$  to more than 600 nm for  $Bi_2WO_{6-x}$  (150 °C, 5 h) induced by the introduction of surface oxygen vacancies.

**Formation and Structure of Surface Oxygen Vacancy.** To investigate the hydrogen reduction process, temperature-programmed reduction (TPR) of the  $Bi_2WO_6$  nanoplates was investigated (Fig. 3a). The  $H_2$ -TPR profile of  $Bi_2WO_6$  sample shows four reduction peaks, the main sharp peak is at about 556 °C, and the other three are at about 323, 746 and 885 °C, respectively. In addition, from the enlarged thermal conductivity detector (TCD) signal in the range of 100 ~ 250 °C (the inset of Fig. 3a), it can be found that two other little reduction peaks emerge at 150 °C and 180 °C, respectively. The six peaks are attributed to the partial loss of oxygen atoms or the reductive decomposition for the  $Bi_2WO_6$  samples, which can be confirmed from the surface atomic concentration obtained from the X-ray photoelectron spectroscopy (XPS) (Table 1) and the X-ray diffraction (XRD) patterns of  $Bi_2WO_6$  and  $Bi_2WO_{6-x}$  samples (Fig. 3b). From Table 1, it can be seen that surface atomic concentration ratio

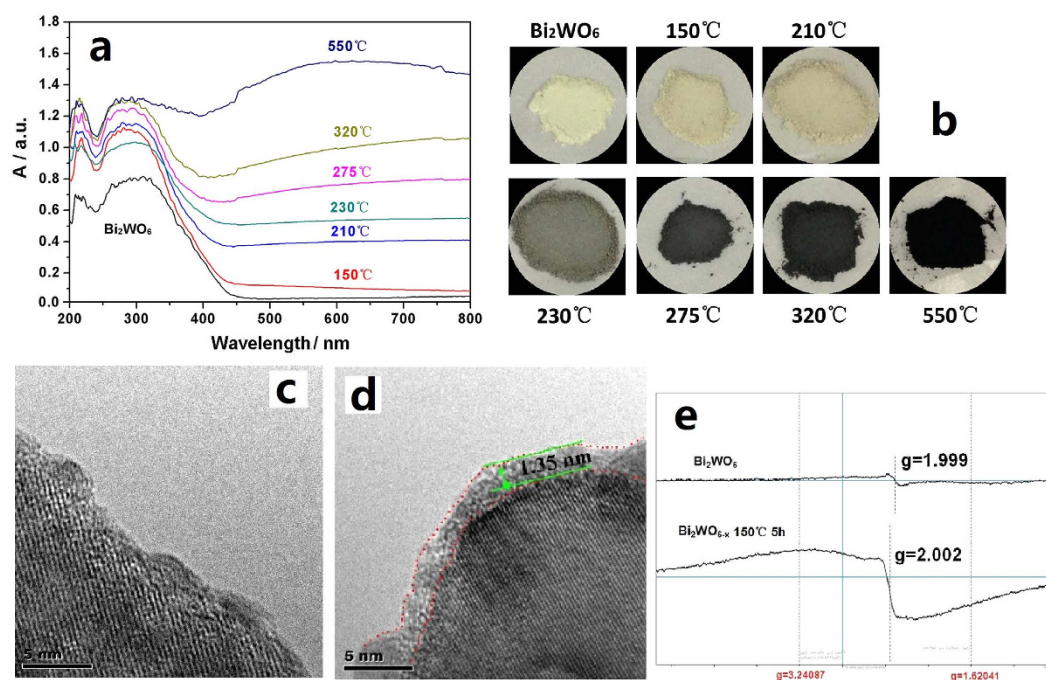


**Figure 4.** (a,b) UV-DRS and the photos of Bi<sub>2</sub>WO<sub>6</sub> and Bi<sub>2</sub>WO<sub>6-x</sub> samples; (c,d) The HR-TEM of Bi<sub>2</sub>WO<sub>6</sub> and Bi<sub>2</sub>WO<sub>6-x</sub> (150 °C for 5 h); (e) *In situ* EPR spectra of Bi<sub>2</sub>WO<sub>6</sub> and Bi<sub>2</sub>WO<sub>6-x</sub> (150 °C for 5 h), at 77 K.

of Bi4f:W4f:O1s changes from 1:0.384:3.07 for pristine Bi<sub>2</sub>WO<sub>6</sub> to 1:0.385:2.90 for Bi<sub>2</sub>WO<sub>6-x</sub>. Compared with Bi<sub>2</sub>WO<sub>6</sub>, the surface atomic concentration ratio of Bi4f:W4f for Bi<sub>2</sub>WO<sub>6-x</sub> (150 °C, 5 h) has hardly any change, but that of Bi4f:O1s obviously increases, indicating that the surface oxygen atoms are removed. This confirms the formation of the surface oxygen vacancies. Fig. 3b shows no phase transformation or any impurity is observed for Bi<sub>2</sub>WO<sub>6-x</sub> samples after hydrogen reduction at temperature range from 150 to 275 °C for 5 h, so here only oxygen atoms are removed from Bi<sub>2</sub>WO<sub>6</sub>, generating oxygen vacancies with different number and degrees. However, after 320 °C 5 h hydrogen reduction, a small amount of metal Bi is generated; even after 550 °C 5 h hydrogen reduction, the Bi-O bonds are ruptured totally and part of the W-O bond was also fractured, thus Bi<sub>2</sub>WO<sub>6</sub> is reduced to the mixture of metal Bi and WO<sub>2.625</sub>. These phenomena are closely related with the structure of Bi<sub>2</sub>WO<sub>6</sub> and the bond energy between two atoms.

From Fig. 3c, it can be visually seen that there are six nonequivalent O atoms in Bi<sub>2</sub>WO<sub>6</sub>, and they are connected with Bi1, Bi2 and W atoms, respectively. Based on the bond length of Bi-O or W-O (supporting information Table S1) and the bond angle of O-Bi-O (or O-W-O) (Table S2)<sup>33</sup>, O atoms should be firstly removed from Bi atoms, then partly leave from W atom, and the losing order is from surface O atoms to bulk O atoms inch by inch, thus generating oxygen vacancies with different number and degrees. This is echo with the results of the H<sub>2</sub>-TPR and XRD of as-prepared samples.

The change of surface chemical bonding of Bi<sub>2</sub>WO<sub>6</sub> photocatalysts before and after hydrogen reduction was investigated with x-ray photoelectron spectroscopy (XPS). The O 1s and Bi 4f XPS spectra of Bi<sub>2</sub>WO<sub>6-x</sub> (150 °C, 5 h) shift to a higher binding energy from 530.20 eV, 159.28 eV to 530.48 eV, 159.41 eV, respectively (Fig. 3d,e), which are contributed to the formation of neighboring oxygen vacancies with a high electron-attracting effect. The W 4f XPS spectra are almost identical Fig. S1, which indicates that W atom have a similar bonding environment after hydrogenation reduction. Furthermore, the O1s peak can be separated into three peaks at 530.05, 530.69 and 532.29 eV. The two lower binding energy centers at 530.05 eV, 530.69 eV belong to the coordination of oxygen in Bi-O and W-O, respectively<sup>34,35</sup>. The higher binding energy centered at 532.29 eV can be attributed to the coordination of oxygen in O-H or adsorbed oxygen<sup>34-36</sup>. It can be clearly found that the contribution of Bi-O is decreased for Bi<sub>2</sub>WO<sub>6-x</sub> (150 °C, 5 h), which results from the removed of the O atom connecting with Bi atom. This phenomenon further confirms the formation of oxygen vacancies and reveals the source of oxygen vacancies.

The UV-DRS of Bi<sub>2</sub>WO<sub>6</sub> and Bi<sub>2</sub>WO<sub>6-x</sub> powders after hydrogen reduction at different temperature were shown in Fig. 4a. The absorbance of as-prepared samples is gradually increased with the enhanced hydrogen reduction temperature. However, the photocatalytic activities are not wholly increase with the enhanced of the hydrogen reduction temperature. Therefore, the conclusion can be drawn that the increase of the absorbance cannot always result in the enhancement of the photoactivity. Here, the largely enhanced absorbance is mainly attributed to the samples color deepened from faint yellow pristine Bi<sub>2</sub>WO<sub>6</sub> to gray-yellow Bi<sub>2</sub>WO<sub>6-x</sub>, finally turn into black powders composed by Bi and WO<sub>2.625</sub> after hydrogen reduction at different temperature (Fig. 4b). This is because the electron-trapped oxygen vacancy can bind one or two electrons, giving rise to singly charged (F<sup>+</sup> centers) or to neutral F<sup>0</sup> center (known as a color center)<sup>37-39</sup>. Nevertheless, although the absorbance of Bi<sub>2</sub>WO<sub>6-x</sub>



Sample	BET (m <sup>2</sup> /g)	Zeta potential (mV)
Bi <sub>2</sub> WO <sub>6</sub>	21.53	0.42
Bi <sub>2</sub> WO <sub>6-x</sub> (150 °C, 5 h)	23.54	-12.80

**Table 2.** The comparison of BET and Zeta potential for Bi<sub>2</sub>WO<sub>6</sub> and Bi<sub>2</sub>WO<sub>6-x</sub> samples.

(150 °C, 5 h) sample only shows a small improvement and the band edge also slightly red-shift, the photocatalytic performance are significantly boosted, which are caused by the generation of surface oxygen vacancies.

From Fig. 4c,d the HR-TEM of Bi<sub>2</sub>WO<sub>6</sub> and Bi<sub>2</sub>WO<sub>6-x</sub> (150 °C, 5 h) samples, it can be intuitively seen that pristine Bi<sub>2</sub>WO<sub>6</sub> reveals perfect lattice features, however, the edge of Bi<sub>2</sub>WO<sub>6-x</sub> (150 °C, 5 h) particles becomes disordered (thickness about 1.35 nm), which indicates that the surface structure of Bi<sub>2</sub>WO<sub>6-x</sub> (150 °C, 5 h) is damaged and surface oxygen vacancies are formed. Electron paramagnetic resonance (EPR) is a sensitive and direct technique to monitor various behaviors to the presence oxygen defects<sup>40</sup>. To further confirm the existence of oxygen vacancy, *in situ* EPR of as-prepared samples was surveyed at 77 K in liquid N<sub>2</sub>, as shown in Fig. 4e. Up to now, *in situ* EPR signal of Bi<sub>2</sub>WO<sub>6</sub> powders has rarely been reported. However, it is reported previously that the g factor ~2.001 is attributed to oxygen vacancy for TiO<sub>2</sub><sup>41,42</sup> and ZnO<sup>43,44</sup>. In this work, the strengthening and broadening of the EPR signal for Bi<sub>2</sub>WO<sub>6-x</sub> (150 °C, 5 h) about g ~2.002 can also be attributed to the electron-trapped center at the site of oxygen vacancies, as reported previously by our group about oxygen-deficient BaAl<sub>2</sub>O<sub>4</sub><sup>45</sup>.

To detect whether the Bi<sub>2</sub>WO<sub>6-x</sub> (150 °C, 5 h) sample contains some hydrogen atoms after hydrogen reduction, the mass spectrum (MS) of hydrogen in the vent gas during the process of H<sub>2</sub>-TPD of Bi<sub>2</sub>WO<sub>6-x</sub> (150 °C, 5 h) were performed. From supporting information Fig. S2, it can be seen that the hydrogen signal has hardly any change in the vent gas, implying that the hydrogen element content in Bi<sub>2</sub>WO<sub>6-x</sub> (150 °C, 5 h) can be negligible. On the other hand, the hydrogen-related defects (O-H) also can be detected and quantitatively estimated by IR spectra. As is well known, the peaks around 3480 cm<sup>-1</sup> and 1620 cm<sup>-1</sup> are OH stretching vibration and bending vibration. However, from the IR spectra of as-prepared samples from 600 nm to 3600 nm (supporting information Fig. S3), it can not find the distinct signal of OH vibration peak. In addition, the 1385 cm<sup>-1</sup> is also expected to be hydrogen-related defects modes, which were expected an additional band of OH vibration<sup>46-48</sup>. Compared with pristine Bi<sub>2</sub>WO<sub>6</sub>, the intensities of 1385 cm<sup>-1</sup> peak signal (hydrogen-related defects) of Bi<sub>2</sub>WO<sub>6-x</sub> (150, 230 °C) show hardly any change (still no signal), indicating that the number of hydrogen-related defects in Bi<sub>2</sub>WO<sub>6-x</sub> (150 °C, 5 h) nanoplates with high photoactivity and photocurrent can be neglected (the inset of Fig. S3). Nevertheless, after hydrogen reduction at 275 °C for 5 h, the Bi<sub>2</sub>WO<sub>6-x</sub> exhibits a little peak at 1385 cm<sup>-1</sup>, implying that it possesses a small number of hydrogen-related defects, which plays a supplementary role in the decrease of the photocatalytic activity<sup>45</sup>.

**Mechanism of Enhanced Photocatalytic Activity and Efficiency.** The photocatalytic mechanism can be elucidated by the trapping experiments of radicals and holes. The main oxidative species in the photocatalytic process could be detected through the trapping experiments of hydroxyl radicals (•OH), holes and superoxide radical (•O<sub>2</sub><sup>-</sup>) by using t-BuOH(•OH scavenger)<sup>49</sup>, HCOOH(hole scavenger)<sup>50</sup> and purging N<sub>2</sub> gas(•O<sub>2</sub><sup>-</sup> scavenger)<sup>51</sup>, respectively. Fig. S4a shows that the photoactivity of Bi<sub>2</sub>WO<sub>6</sub> is greatly prevented by the addition of HCOOH, however, the addition of t-BuOH and purging of N<sub>2</sub> gas only cause a small change in the photodegradation of 2, 4-DCP. The result suggests that the photogenerated holes are the main oxidative species of Bi<sub>2</sub>WO<sub>6</sub> system. On the other hand, the photoactivity is also greatly inhibited by the addition of HCOOH in Bi<sub>2</sub>WO<sub>6-x</sub> (150 °C, 5 h) system (Fig. S4b), so the main oxidative species is also holes, which is the same as that of in pristine Bi<sub>2</sub>WO<sub>6</sub> system. •O<sub>2</sub><sup>-</sup> and •OH play the assistant role. Therefore, the photocatalytic degradation mechanism of Bi<sub>2</sub>WO<sub>6-x</sub> (150 °C, 5 h) on 2, 4-DCP is not changed and the main oxidative species is still holes.

As discussed above, the degradation mechanism of Bi<sub>2</sub>WO<sub>6-x</sub> (150 °C, 5 h) is the same as that of pristine Bi<sub>2</sub>WO<sub>6</sub>, and the particle size, the crystal phase structure (from the XRD spectra, as shown in Fig. 3b) are not distinctly changed. The small enhanced adsorption ability for 2, 4-DCP from 4% of Bi<sub>2</sub>WO<sub>6</sub> to 10% of Bi<sub>2</sub>WO<sub>6-x</sub> (150 °C, 5 h) as shown in Fig. S5 is resulted from the slightly enlarged of the surface area (Bi<sub>2</sub>WO<sub>6</sub>: 21.53 m<sup>2</sup>/g; Bi<sub>2</sub>WO<sub>6-x</sub> (150 °C, 5 h): 23.45 m<sup>2</sup>/g) and the decrease of the zeta potential (Bi<sub>2</sub>WO<sub>6</sub>: 0.42 mV; Bi<sub>2</sub>WO<sub>6-x</sub> (150 °C, 5 h): -12.80 mV) (as shown in Table 2) due to the formation of surface oxygen vacancies, which is in favor of the enhanced photoactivity.

The separation efficiency of photogenerated electron and hole pairs also plays an important role in the enhancement of photocatalytic activity, which can be investigated by the typical electrochemical impedance spectroscopy (EIS). Fig. 5a shows the EIS responses of pristine Bi<sub>2</sub>WO<sub>6</sub> and Bi<sub>2</sub>WO<sub>6-x</sub> electrodes with and without visible irradiation. In each case, there is one arc on the EIS plane, indicating that the surface charge transfer is the rate-determining step in the photocatalytic reaction. A necessary step for semiconductor photocatalytic performance is the generation and separation of photogenerated electron-hole pairs. The arc radiuses of the Bi<sub>2</sub>WO<sub>6-x</sub> (150 and 180 °C) electrode both are smaller than that of the pristine Bi<sub>2</sub>WO<sub>6</sub> electrode regardless of whether with or without visible-light irradiation, and the order is Bi<sub>2</sub>WO<sub>6-x</sub> (150 °C) < Bi<sub>2</sub>WO<sub>6-x</sub> (180 °C) < pristine Bi<sub>2</sub>WO<sub>6</sub>. The smaller the arc radius of an EIS Nyquist plot, the higher the efficiency of charge separation<sup>52,53</sup>. Thus, in the case of Bi<sub>2</sub>WO<sub>6-x</sub>, the photogenerated electron-hole pairs are easier separated and transferred to the samples surface, and the photoactivities both are higher than that of pristine Bi<sub>2</sub>WO<sub>6</sub>. Therefore, the enhanced photocatalytic performance is mainly attributed to the increase of the charge separation efficiency due to the broadening of the valence band (VB) width induced by surface oxygen-vacancy states, which will be discussed in the following part.

Furthermore, the photocurrent also can be considered as an indicator of the recombination rate of photogenerated electron-hole pairs<sup>37</sup>. Under visible light, the photocurrent densities of Bi<sub>2</sub>WO<sub>6-x</sub> (hydrogen reduction at

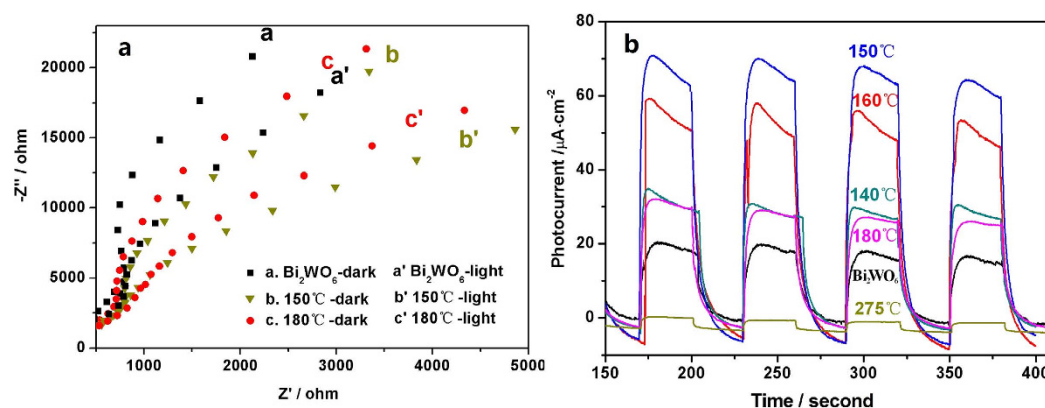


**Figure 5.** (a) EIS of pristine  $\text{Bi}_2\text{WO}_6$  and  $\text{Bi}_2\text{WO}_{6-x}$  (150 and  $180^\circ\text{C}$ , 5 h) after deposition on ITO electrodes, with and without visible light irradiation ( $\lambda > 420\text{ nm}$ ); (b) Photocurrents of  $\text{Bi}_2\text{WO}_6$  and  $\text{Bi}_2\text{WO}_{6-x}$  samples after deposition on ITO electrodes, under visible light ( $\lambda > 420\text{ nm}$ ).

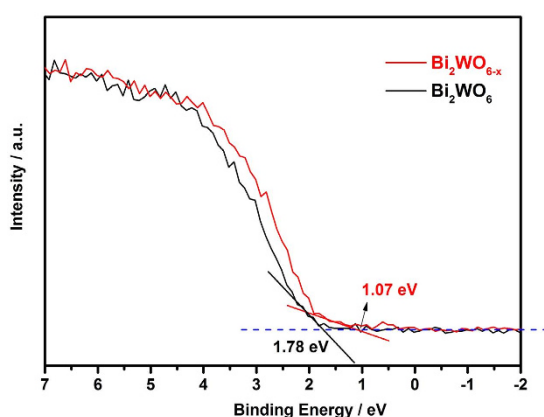


**Figure 6.** Valence-band XPS spectra of the pristine  $\text{Bi}_2\text{WO}_6$  and  $\text{Bi}_2\text{WO}_{6-x}$  ( $150^\circ\text{C}$  for 5 h).

140, 150, 160,  $180^\circ\text{C}$ , respectively) electrodes are all higher at different level than that of pristine  $\text{Bi}_2\text{WO}_6$  electrode (Fig. 5b). Especially,  $\text{Bi}_2\text{WO}_{6-x}$  (reduction at  $150^\circ\text{C}$ ) shows the highest photocurrent, which is about 3.5 times as high as that of pristine  $\text{Bi}_2\text{WO}_6$ . However,  $\text{Bi}_2\text{WO}_{6-x}$  (reduction at  $275^\circ\text{C}$ ) electrode shows slightly lower photocurrent than that of pristine  $\text{Bi}_2\text{WO}_6$  electrode. The enhanced or reduced photocurrents demonstrate that the increase or decrease of the photogenerated carriers transport rate, which are associated with the number and kind of oxygen vacancies. These results are well consistent with the change (improve or reduce) of the photocatalytic activities for the as-prepared samples (Fig. 1a) and the EIS plot (Fig. 5a).

The density of states (DOS) of the valence band of  $\text{Bi}_2\text{WO}_6$  photocatalysts were measured by the valence band XPS. The  $\text{Bi}_2\text{WO}_6$  displays valence band DOS with the edge of the maximum energy at about 1.78 eV, however, the edge of the valence band energy for  $\text{Bi}_2\text{WO}_{6-x}$  ( $150^\circ\text{C}$ , 5 h) shifts toward the vacuum level at approximately 1.07 eV (Fig. 6), indicating the valence band maximum rise with low density of states.

Based on the above discussions, the proposed schematic diagram for the mechanism of the enhanced photocatalytic activity and the efficiency of  $\text{Bi}_2\text{WO}_{6-x}$  photocatalyst are provided in Fig. 7. Surface oxygen vacancy is a shallow defect, which may be below the conduction band minimum (CBM) or above the valence band maximum (VBM). It was reported previously by Jung and coauthor that the rising of VBM and the reduced of band gap over anatase  $\text{TiO}_2$  from O-terminated surface to Ti-termination surface has been observed image by the scanning tunneling microscopy<sup>54</sup>. The band gap of  $\text{LiTi}_2(\text{PO}_4)_3$  significantly reduced due to the formation of oxygen-vacancy states above the valence band, under poor oxygen conditions<sup>55</sup>. And our group also has been found that the surface oxygen-defects states will be generated on the VBM for  $\text{ZnO}$  and  $\text{BiPO}_4$  through experimental and theoretical calculation<sup>28–30,56</sup>. Furthermore, the work shows that the photoresponse wavelength range is extended as well as the photoactivity is enhanced for  $\text{Bi}_2\text{WO}_{6-x}$  photocatalyst. The extending of the photoresponse wavelength range (from 450 nm to about 600 nm) can be attributed to the shallow surface oxygen-vacancy states above and partly overlapping with the VB of  $\text{Bi}_2\text{WO}_6$ , resulting in the rise of the VBM. Simultaneously, the rising of the VBM also can results in the expanding the VB width. Therefore, the transport rate of photogenerated carriers improved, leading to the enhancement of separation efficiency of photogenerated electron-hole pairs, thus the photocatalytic performance also is improved.

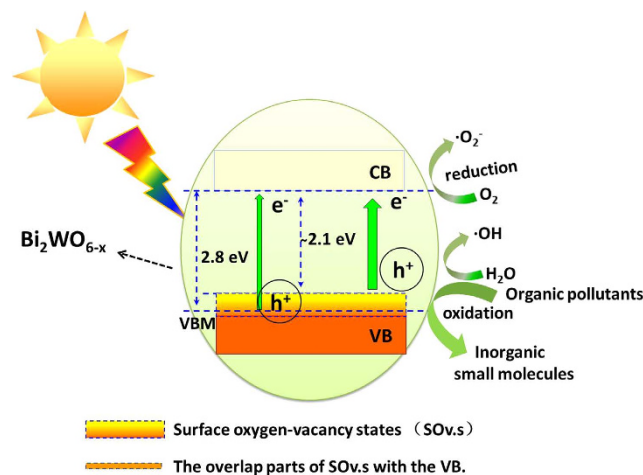


**Figure 7.** Schematic diagram illustrating the mechanism of charge separation and photocatalytic reaction of  $\text{Bi}_2\text{WO}_{6-x}$  photocatalyst, under sun light irradiation.

In summary, the visible photoresponse range was extended and the photoactivity was also enhanced for  $\text{Bi}_2\text{WO}_6$  nanoplates via surface oxygen vacancies. The visible-light wavelength range is expanded from 450 nm for pristine  $\text{Bi}_2\text{WO}_6$  to 600 nm for  $\text{Bi}_2\text{WO}_{6-x}$ . The photoactivity of  $\text{Bi}_2\text{WO}_{6-x}$  (150 °C, 5 h) is 2.1 times as high as that of pristine  $\text{Bi}_2\text{WO}_6$ . The expanded the visible-light range and the enhanced photoactivity both are resulted from the production of the surface oxygen vacancies. These are because surface oxygen-defect states are located above and partly overlapping with the VB, resulting in the rising of the valence band maximum with low density of states and the broadening of the VB. Furthermore, the generation of oxygen vacancies also can slightly increase the adsorbance on 2, 4-DCP, which is a supplement to the enhanced of the photoactivity.

## Methods

**Preparation of photocatalysts.** Square  $\text{Bi}_2\text{WO}_6$  nanoplates (surface area 21.53 m<sup>2</sup>/g) were synthesized by the simple hydrothermal method<sup>14</sup>.  $\text{Bi}_2\text{WO}_6$  with oxygen vacancy samples were prepared as follows: (1) the temperature programmed reduction (TPR) measurement (ChemiSorb 2720, Micromeritics, America) using hydrogen gas was performed in a specially designed quartz tube with 0.073 g of  $\text{Bi}_2\text{WO}_6$ . (2) Based on the  $\text{H}_2$ -TPR graph, hydrogen reduction process was performed to prepare oxygen-vacancy  $\text{Bi}_2\text{WO}_6$  samples. Firstly, the synthesized  $\text{Bi}_2\text{WO}_6$  samples were pretreated by He gas at 120 °C for 2 h. Then  $\text{H}_2$ /Ar mixture gas was introduced and the temperature from 25 ± 0.5 °C to designed temperature at a rising rate of 10 °C · min<sup>-1</sup>, the time was kept for 1 ~ 9 h at 2 h intervals. Finally, the samples were cooled down to room temperature naturally, maintaining  $\text{H}_2$ /Ar mixture gas.

**Characterization.** Ultraviolet–visible diffuse reflectance spectroscopy (UV–DRS) was performed on Hitachi U–3010,  $\text{BaSO}_4$  was used as reference. The crystallinity and purity of the as-prepared samples was characterized by X-ray diffraction (XRD) on Bruker D8-advance diffractometer using Cu K $\alpha$  radiation ( $\lambda = 1.5418 \text{ \AA}$ ). X-Ray photoelectron spectroscopy (XPS) was obtained using a Quantera (ULVAC-PHI, Japan). An Al K $\alpha$  X-ray source with a power of 25 W was used. The pass energy of the analyzer was set at 37.25 eV and the base pressure of the analysis chamber was better than  $4 \times 10^{-8}$  Torr. The binding energies were referenced to the C1s line at 284.8 eV from adventitious carbon. For our XPS data, all curves were defined as 20% Lorentzian, 80% Gaussian. The curve fitting was done using XPSpeak software, with Newton's iteration method and 300 iterations. A high-resolution transmission electron microscope (HR-TEM, JEM 2010F) were operated at an accelerating voltage of 200 kV. *In situ* electron paramagnetic resonance (EPR) measurement was carried out using an endor spectrometer (JEOL ES-ED3X) at 77 K in liquid nitrogen. The g factor was obtained by taking the signal of manganese as standard. Atmospheric gas analysis system (HIDEN QIC20-MS) was utilized to survey the hydrogen in the vent gas formed in the process of  $\text{H}_2$ -TPD of  $\text{Bi}_2\text{WO}_{6-x}$  (150 °C for 5 h). The photocurrents and electrochemical impedance spectroscopy (EIS) were measured on an electrochemical system (CHI-660B, China). Surface area was determined with the Brunauer–Emmett–Teller (BET) method, porosity measurements (TriStar II3020, Micromeritics). The zeta potentials were measured by the monitor particle method using an electrophoretic light scattering spectrophotometer (Size-100, Horiba).

**Catalytic Evaluation.** The photocatalytic performances of as-prepared samples were evaluated by the decomposition of 2, 4-DCP, in solution under visible light and simulated solar irradiation. Visible light source was obtained from a 500 W Xe lamp with a 420 nm cutoff filter. Simulated solar irradiation was obtained from the Xe lamp with an AM1.5 filter. 25 mg photocatalyst was added into prepared 50 mL 15 ppm of 2, 4-DCP aqueous solution. Before the light irradiation, the suspensions were firstly ultrasonic dispersed in dark for 10 min, then magnetically stirred for 15 min to reach the adsorption–desorption equilibrium. At given time intervals, 3 mL aliquots were sampled and centrifuged to remove the photocatalyst particles. Synchronously, the filtrated 2, 4-DCP solutions were analyzed by the HPLC (Lumtech) analysis with a UV detector at 284 nm. The Venusil

XPB-C18 reversed phase column was used. The mobile phase was methanol and water (75:25, v/v) with a flow rate of  $1.0 \text{ mL} \cdot \text{min}^{-1}$ .

Photoelectrochemical measurements were carried out in a conventional three-electrode system. ITO/ $\text{Bi}_2\text{WO}_6$  or ITO/ $\text{Bi}_2\text{WO}_{6-x}$  electrodes served as the working electrode. A platinum wire as counter electrode and a standard calomel electrode (SCE) as reference electrode were utilized in the photoelectric studies.  $0.1 \text{ M Na}_2\text{SO}_4$  was used as the electrolyte solution. ITO/ $\text{Bi}_2\text{WO}_6$  or ITO/ $\text{Bi}_2\text{WO}_{6-x}$  electrodes were prepared by a dip-coating method: 5 mg of photocatalyst was suspended in 1 mL deionized water to make slurry, and then the slurry was dip-coated onto a  $2 \text{ cm} \times 4 \text{ cm}$  ITO glass electrode. The as-prepared electrodes were naturally dried and subsequently calcined at  $80^\circ\text{C}$  for 5 h in vacuum drying oven. All investigated electrodes were of similar thickness ( $0.8\text{--}1 \mu\text{m}$ ).

## References

- Mahanty, S. & Ghose, J. Preparation and Optical Studies of Polycrystalline  $\text{Bi}_2\text{WO}_6$ . *Mater. Lett.* **11**, 254–256 (1991).
- Jimenez, R., Castro, A. & Jimenez, B. Evidence of Ferroelastic–Ferroelastic Phase Transition in  $\text{BiMo}_x\text{W}_{1-x}\text{O}_6$  Compounds. *Appl. Phys. Lett.* **83**, 3350–3352 (2003).
- Castro, A. *et al.* New  $\text{Bi}_2\text{Mo}_{1-x}\text{W}_x\text{O}_6$  Solid Solution: Mechano-synthesis, Structural Study, and Ferroelectric Properties of the  $x = 0.75$  Member. *Chem. Mater.* **15**, 3395–3401 (2003).
- Murugan, G. S. & Varma, K. B. R. Dielectric, Linear and Non-Linear Optical Properties of Lithium Borate–Bismuth Tungstate Glasses and Glass–Ceramics. *J. Non-Cryst. Solids* **279**, 1–13 (2001).
- Luo, S., Noguchi, Y., Miyayama, M. & Kudo, T. Rietveld Analysis and Dielectric Properties of  $\text{Bi}_2\text{WO}_6\text{--Bi}_4\text{Ti}_3\text{O}_{12}$  Ferroelectric System. *Mater. Res. Bull.* **36**, 531–540 (2001).
- Murugan, G. S., Subbanna, G. N. & Varma, K. B. R. Nanocrystallization of Ferroelectric Bismuth Tungstate in Lithium Borate Glass Matrix. *J. Mater. Sci. Lett.* **18**, 1687–1690 (1999).
- Bordun, O. M. Luminescence Centers in  $\text{Bi}_2\text{WO}_6$  and  $\text{Bi}_2\text{W}_2\text{O}_9$  Thin Films. *Inorg. Mater.* **34**, 1270–1272 (1998).
- Shi, Y. H., Feng, S. H. & Cao, C. S. Hydrothermal Synthesis and Characterization of  $\text{Bi}_2\text{MoO}_6$  and  $\text{Bi}_2\text{WO}_6$ . *Mater. Lett.* **44**, 215–218 (2000).
- Shang, M. *et al.*  $\text{Bi}_2\text{WO}_6$  Nanocrystals with High Photocatalytic Activities under Visible Light. *J. Phys. Chem. C* **112**, 10407–10411 (2008).
- Shi, R., Huang, G. L., Lin, J. & Zhu, Y. F. Photocatalytic Activity Enhancing for  $\text{Bi}_2\text{WO}_6$  by Fluorine Substitution. *J. Phys. Chem. C* **113**, 19633–19638 (2009).
- Kudo, A. & Hijii, S.  $\text{H}_2$  or  $\text{O}_2$  Evolution from Aqueous Solutions on Layered Oxide Photocatalysts Consisting of  $\text{Bi}^{3+}$  with  $6s^2$  Configuration and  $d^0$  Transition Metal Ions. *Chem. Lett.* **28**, 1103–1104 (1999).
- Tang, J. W., Zou, Z. G. & Ye, J. H. Photocatalytic Decomposition of Organic Contaminants by  $\text{Bi}_2\text{WO}_6$  under Visible Light Irradiation. *Catal. Lett.* **92**, 53–56 (2004).
- Zhang, L. S., Wang, W. Z., Zhou, L. & Xu, H. L.  $\text{Bi}_2\text{WO}_6$  Nano- and Microstructures: Shape Control and Associated Visible-Light-Driven Photocatalytic Activities. *Small* **3**, 1618–1625 (2007).
- Zhang, C. & Zhu, Y. F. Synthesis of Square  $\text{Bi}_2\text{WO}_6$  Nanoplates as High-Activity Visible-Light-Driven Photocatalysts. *Chem. Mater.* **17**, 3537–3545 (2005).
- Fu, H. B. *et al.* Synthesis, Characterization and Photocatalytic Properties of Nanosized  $\text{Bi}_2\text{WO}_6$ ,  $\text{PbWO}_4$  and  $\text{ZnWO}_4$  Catalysts. *Mater. Res. Bull.* **42**, 696–706 (2007).
- Xiao, Q. *et al.* Photocatalytic Degradation of Methylene Blue over  $\text{Co}_3\text{O}_4/\text{Bi}_2\text{WO}_6$  Composite under Visible Light Irradiation. *Catal. Commun.* **9**, 1247–1253 (2008).
- Zhang, L. S. *et al.* AgBr–Ag– $\text{Bi}_2\text{WO}_6$  Nanojunction System: A Novel and Efficient Photocatalyst with Double Visible-Light Active Components. *Appl. Catal. A* **363**, 221–229 (2009).
- Zhang, Z. J. *et al.* Inducing Photocatalysis by Visible Light Beyond the Absorption Edge: Effect of Upconversion Agent on the Photocatalytic Activity of  $\text{Bi}_2\text{WO}_6$ . *Appl. Catal. B* **101**, 68–73 (2010).
- Tian, Na. *et al.* Influences of Gd Substitution on the Crystal Structure and Visible-Light-Driven Photocatalytic Performance of  $\text{Bi}_2\text{WO}_6$ . *J. Phys. Chem. C* **118**, 15640–15648 (2014).
- Zhu, S. B. *et al.* Synergetic Effect of  $\text{Bi}_2\text{WO}_6$  Photocatalyst with  $\text{C}_{60}$  and Enhanced Photoactivity under Visible Irradiation. *Environ. Sci. Technol.* **41**, 6234–6239 (2007).
- Li, Y. Y. *et al.* Carbon-modified  $\text{Bi}_2\text{WO}_6$  nanostructures with improved photocatalytic activity under visible light. *Dalton Trans.* **39**, 3420–3425 (2010).
- Zhang, Z. J. *et al.* Photocatalysis Coupled with Thermal Effect Induced by SPR on Ag-Loaded  $\text{Bi}_2\text{WO}_6$  with Enhanced Photocatalytic Activity. *J. Phys. Chem. C* **116**, 25898–25903 (2012).
- Huang, H. W. *et al.* Ce and F Comodification on the Crystal Structure and Enhanced Photocatalytic Activity of  $\text{Bi}_2\text{WO}_6$  Photocatalyst under Visible Light Irradiation. *J. Phys. Chem. C* **118**, 14379–14387 (2014).
- Chen, X. B., Liu, L., Yu, P. Y. & Mao, S. S. Increasing Solar Absorption for Photocatalysis with Black Hydrogenated Titanium Dioxide Nanocrystals. *Science* **331**, 746–750 (2011).
- Wang, G. M. *et al.* Hydrogen-Treated  $\text{TiO}_2$  Nanowire Arrays for Photoelectrochemical Water Splitting. *Nano Lett.* **11**, 3026–3033 (2011).
- Asok, A., Gandhi, M. N. & Kulkarni, A. R. Enhanced Visible Photoluminescence in  $\text{ZnO}$  Quantum Dots by Promotion of Oxygen Vacancy Formation. *Nanoscale* **4**, 4943–4946 (2012).
- Xing, M. Y., Zhang, J. L., Chen, F. & Tian, B. Z. An Economic Method to Prepare Vacuum Activated Photocatalysts with High Photo-Activities and Photosensitivities. *Chem. Commun.* **47**, 4947–4949 (2011).
- Ly, Y. H. *et al.* Production of Visible Activity and UV Performance Enhancement of  $\text{ZnO}$  Photocatalyst via Vacuum Deoxidation. *Appl. Catal. B* **138**, 26–32 (2013).
- Ly, Y. H., Zhu, Y. Y. & Zhu, Y. F. Enhanced Photocatalytic Performance for  $\text{BiPO}_4$  Nanorod Induced by Surface Oxygen Vacancy. *J. Phys. Chem. C* **117**, 18520–18528 (2013).
- Ly, Y. H., Liu, Y. F., Zhu, Y. Y. & Zhu, Y. F. Surface Oxygen Vacancy Induced the Photocatalytic Performance Enhancement of  $\text{BiPO}_4$  Nanorod. *J. Mater. Chem. A* **2**, 1174–1182 (2014).
- Kong, M. *et al.* Tuning the Relative Concentration Ratio of Bulk Defects to Surface Defects in  $\text{TiO}_2$  Nanocrystals Leads to High Photocatalytic Efficiency. *J. Am. Chem. Soc.* **133**, 16414–16417 (2011).
- Endo, T., Kobayashi, T., Sato, T. & Shimada, M. High-pressure Synthesis and Electrical-Properties of  $\text{BaTiO}_3\text{--XFX}$ . *J. Mater. Sci.* **25**, 619–623 (1990).
- Islam, M. S. *et al.* Structural and Computational Studies of  $\text{Bi}_{(2)}\text{WO}_{(6)}$  Based Oxygen Ion Conductors. *J. Mater. Chem.* **8**, 655–660 (1998).
- Wang, D. J. *et al.* Synthesis of mesoporous  $\text{Bi}_2\text{WO}_6$  architectures and their gas sensitivity to ethanol. *J. Mater. Chem. C* **1**, 4153–4162 (2013).
- Yang, W. J. *et al.* Enhanced photosensitized activity of a  $\text{BiOCl--Bi}_2\text{WO}_6$  heterojunction by effective interfacial charge transfer. *Phys. Chem. Chem. Phys.* **15**, 19387–19394 (2013).



36. Zhou, Y. *et al.* High-Yield Synthesis of Ultrathin and Uniform Bi<sub>2</sub>WO<sub>6</sub> Square Nanoplates Benefitting from Photocatalytic Reduction of CO<sub>2</sub> into Renewable Hydrocarbon Fuel under Visible Light. *ACS Appl. Mater. Interfaces* **3**, 3594–3601 (2011).
37. Scharfschwerdt, R. *et al.* Oxygen Vacancies in BaTiO<sub>3</sub>. *Phys. Rev. B* **54**, 15284–15290 (1996).
38. Laguta, V. V. *et al.* Electron Spin Resonance Investigation of Oxygen-Vacancy-Related Defects in BaTiO<sub>3</sub> Thin Films. *Appl. Phys. Lett.* **87**, 022903(1–3) (2005).
39. Kakazev, N. G., Sreckovic, T. V. & Ristic, M. M. Electronic Paramagnetic Resonance Investigation of the Evolution of Defects in Zinc Oxide during Tribophysical Activation. *J. Mater. Sci.* **32**, 4619–4622 (1997).
40. Alim, K. A. *et al.* Electron Spin Resonance Investigation of Oxygen-Vacancy-Related Defects in BaTiO<sub>3</sub> Thin Films. *J. Appl. Phys.* **97**, 124313(1–3) (2005).
41. Howe, R. F. & Gratzel, M. Electron-Paramagnetic-Res Study of Hydrated Anatase under UV Irradiation. *J. Phys. Chem.* **91**, 3906–3909 (1987).
42. Nakaoka, Y. & Nosaka, Y. ESR Investigation into the Effects of Heat Treatment and Crystal Structure on Radicals Produced over Irradiated TiO<sub>2</sub> Powder. *J. Photochem. Photobiol. A* **110**, 299–305 (1997).
43. Kasai, P. H. Electron Spin Resonance Studies of Donors and Acceptors in ZnO. *Phys. Rev.* **130**, 989–995 (1963).
44. Ischenko, V. *et al.* Zinc Oxide Nanoparticles with Defects. *Adv. Funct. Mater.* **15**, 1945–1954 (2005).
45. Zhang, L. W., Wang, L. & Zhu, Y. F. Synthesis and Performance of BaAl<sub>2</sub>O<sub>4</sub> with a Wide Spectral Range of Optical Absorption. *Adv. Funct. Mater.* **17**, 3781–3790 (2007).
46. Abbas, H. & Nasser, S. A. Hydroxyl as a Defect of the Manganese Dioxide Lattice and its Applications to the Dry Cell Battery. *J. Power Sources* **58**, 15–21 (1996).
47. Shi, R. *et al.* Synthesis of ZnWO<sub>4</sub> Nanorods with [100] Orientation and Enhanced Photocatalytic Properties. *Appl. Catal. B.* **100**, 173–178 (2010).
48. Pan, C. S., Xu, J., Chen, Y. & Zhu, Y. F. Influence of OH-Related Defects on the Performances of BiPO<sub>4</sub> Photocatalyst for the Degradation of Rhodamine B. *Appl. Catal. B.* **115**, 314–319 (2012).
49. Lee, H. & Choi, W. Photocatalytic Oxidation of Arsenite in TiO<sub>2</sub> Suspension: Kinetics and Mechanisms. *Environ. Sci. Technol.* **36**, 3872–3878 (2002).
50. Tan, T., Beydoun, D. & Amal, R. Effects of Organic Hole Scavengers on the Photocatalytic Reduction of Selenium Anions. *J. Photochem. Photobiol. A* **159**, 273–280 (2003).
51. Pan, C. S. & Zhu, Y. F. New Type of BiPO<sub>4</sub> Oxy-Acid Salt Photocatalyst with High Photocatalytic Activity on Degradation of Dye. *Environ. Sci. Technol.* **44**, 5570–5574 (2010).
52. Leng, W. H. *et al.* Investigation of the Kinetics of a TiO<sub>2</sub> Photoelectrocatalytic Reaction Involving Charge Transfer and Recombination through Surface States by Electrochemical Impedance Spectroscopy. *J. Phys. Chem. B* **109**, 15008–15023 (2005).
53. Liu, H. *et al.* An Alternative Approach to Ascertain the Rate-Determining Steps of TiO<sub>2</sub> Photoelectrocatalytic Reaction by Electrochemical Impedance Spectroscopy. *J. Phys. Chem. B* **107**, 8988–8996 (2003).
54. Dette, C. *et al.* TiO<sub>2</sub> Anatase with a Bandgap in the Visible Region. *NanoLett.* **14**(11), 6533–6538 (2014).
55. Chen, L. J. *et al.* Oxygen Vacancy in LiTiPO<sub>3</sub> and LiTi<sub>2</sub>(PO<sub>4</sub>)<sub>3</sub>: A First-Principles Study. *Phys. Lett. A* **375**, 934–938 (2011).
56. Lv, Y. H. *et al.* Surface Oxygen Vacancy Induced Visible Activity and Enhanced UV Activity of ZnO<sub>1-x</sub> Photocatalyst. *Catal. Sci. Technol.* **3**, 3136–3146 (2013).

## Acknowledgements

This work was partly supported by the National Basic Research Program of China (973 Program) (2013CB632403), National High Technology Research and Development Program of China (863 Program) (2012AA062701) and National Natural Science Foundation of China (21373121, 51472081).

## Author Contributions

Y.L. designed the project, performed the material preparation, characterizations and the photocatalytic performance measurement. W.Y. and R.Z. characterize the photocatalyst. Y.Z. proposed and planned the project. All authors were contributed to discussion and writing the manuscript.

## Additional Information

**Supplementary information** accompanies this paper at <http://www.nature.com/srep>

**Competing financial interests:** The authors declare no competing financial interests.

**How to cite this article:** Lv, Y. *et al.* Fabrication of Wide-Range-Visible Photocatalyst Bi<sub>2</sub>WO<sub>6-x</sub> nanoplates via Surface Oxygen Vacancies. *Sci. Rep.* **6**, 19347; doi: 10.1038/srep19347 (2016).



This work is licensed under a Creative Commons Attribution 4.0 International License. The images or other third party material in this article are included in the article's Creative Commons license, unless indicated otherwise in the credit line; if the material is not included under the Creative Commons license, users will need to obtain permission from the license holder to reproduce the material. To view a copy of this license, visit <http://creativecommons.org/licenses/by/4.0/>